

# Molecularly Thin Polyaramid Nanomechanical Resonators

Hagen Gress,<sup>1</sup> Cody L. Ritt,<sup>2</sup> Inal Shomakhov,<sup>1</sup> Kaan Altmisdort,<sup>1</sup> Michelle Quien,<sup>3</sup> Zitang Wei,<sup>3</sup> John R. Lawall,<sup>4</sup> Narasimha Boddeti,<sup>5</sup> Michael S. Strano,<sup>3,\*</sup> J. Scott Bunch,<sup>1,\*</sup> and Kamil L. Ekinci<sup>1,\*</sup>

<sup>1</sup>*Department of Mechanical Engineering,  
Division of Materials Science and Engineering, and the Photonics Center,  
Boston University, Boston, Massachusetts 02215, USA*

<sup>2</sup>*Department of Chemical and Biological Engineering, University of Colorado Boulder, Boulder, Colorado 80309, USA*

<sup>3</sup>*Department of Chemical Engineering, Massachusetts Institute of Technology,  
Cambridge, Massachusetts 02139, USA*

<sup>4</sup>*National Institute of Standards and Technology, Gaithersburg, Maryland 20899, USA*

<sup>5</sup>*Washington State University, School of Mechanical and Materials Engineering,  
Pullman, Washington 99163, USA*

(Dated: January 16, 2026)

**Abstract:** Two-dimensional polyaramids exhibit strong hydrogen bonding to create molecularly thin nanosheets analogous to graphene. Here, we report the first nanomechanical resonators made out of a two-dimensional polyaramid, 2DPA-1, with thicknesses as small as 8 nm. To fabricate these molecular-scale resonators, we transferred nanofilms of 2DPA-1 onto chips with previously-etched arrays of circular microwells. We then characterized the thermal resonances of these resonators under different conditions. When there is no residual gas inside the 2DPA-1-covered microwells, the eigenfrequencies are well-described by a tensioned plate theory, providing the Young's modulus and tension of the 2DPA-1 nanofilms. With gas present, the nanofilms bulge up and mechanical resonances are modified due to the adhesion, bulging and slack present in the system. The fabrication and mechanical characterization of these first 2DPA-1 nanomechanical resonators represent a convincing path toward molecular-scale polymeric NEMS with high mechanical strength, low density, and synthetic processability.

Keywords: NEMS, 2D material, polymer, nanomechanical resonator, Brownian motion, adhesion energy

Nanoelectromechanical Systems (NEMS) or nanomechanical resonators are evolving both in functionality and form since the first NEMS devices etched out of silicon in the 1990s [1, 2]. An overarching research theme in the field has been the exploration of different materials for NEMS. New materials with extraordinary properties have allowed for superior resonator parameters as well as the reduction of resonator linear dimensions. NEMS made out of one- and two-dimensional (2D) nanomaterials — with unique mechanical, electronic, chemical, and optical properties — have opened the door for devices with linear dimensions well below the limits of lithography and functionalities well beyond those of semiconductors and metals [3–5]. So far, 2D NEMS have been fabricated from a variety of 2D crystalline nanomaterials, such as graphene [6], hexagonal boron nitride [7], transition metal dichalcogenides [8, 9], MXenes [10, 11], and nanoparticles [12–14]. Various polymeric materials have also been explored as mechanical resonators [15–20] — although these structures have typically remained far from molecular scale thicknesses. Converging these two approaches, i.e., creating molecular scale polymeric NEMS analogous to 2D crystalline NEMS, would open up a powerful new direction in the NEMS field.

Recently, a 2D polyaramid, called 2DPA-1 [21], was

synthesized. Molecular-scale disks of 2DPA-1 form by polycondensation of melamine and trimesoyl chloride in solution and assemble into aligned layers upon spin coating (Figure 1a). Each molecular layer is approximately  $\sim 3.7 \text{ \AA} (= 370 \text{ pm})$  thick and stacks via hydrogen bonding to form near-molecular-thickness films with an rms surface roughness of 500 pm [21, 22]. Despite lacking crystallinity, these films possess mechanical and gas barrier properties that are closer to 2D crystalline nanomaterials, such as graphene, than conventional polymers [22], and can be transferred onto substrates just like graphene. In short, 2DPA-1 combines material properties of conventional 1D polymers and 2D inorganic crystalline nanomaterials, such as graphene; it also opens up a new class of 2D nanomaterials that can be tailored to specific applications using the tools of organic chemistry [23, 24]. Such tunability — for example, in gas permeability or in the incorporation of functional groups — could enable a wide range of future technologies requiring high sensitivity and selectivity. This motivates an exploration of various nanoscale devices that can be fabricated from these new 2D polymeric materials. To this end, we report the fabrication and measurement of the first nanomechanical resonators made out of 2DPA-1. In addition to demonstrating nanomechanical resonances, we determine the Young's modulus from the measured resonances; we also develop a mechanical model for a membrane resonator partially adhered to walls and estimate the adhesion energy (between the polymer and the substrate) from resonance frequencies of membranes delaminating from the

\* Email: strano@mit.edu

\* Email: bunch@bu.edu

\* Email: ekinci@bu.edu

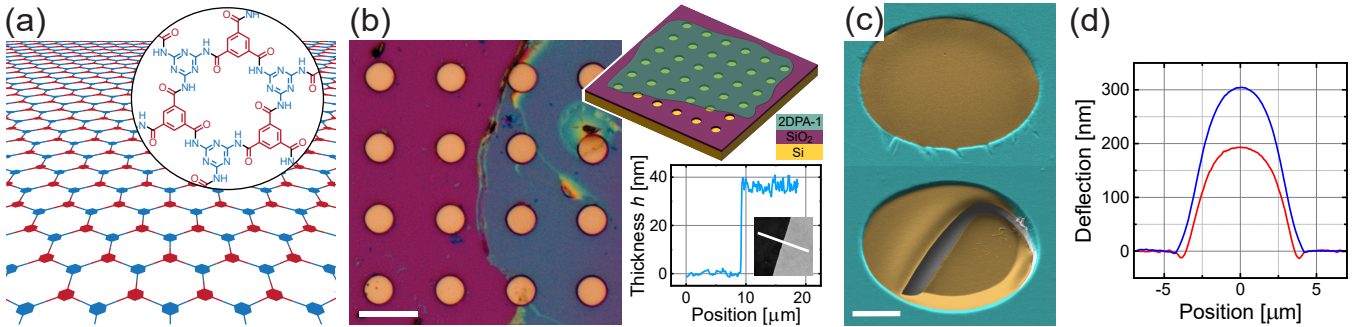


FIG. 1. (a) Illustration of an ideal 2DPA-1 monolayer with the molecular structure shown in the inset. (b) Optical microscope image of a typical sample showing the edge of the 2DPA-1 film. Microwells are etched into the  $\text{SiO}_2$  layer on top of a Si substrate. A 2DPA-1 film is then transferred onto the chip through a wet process to create suspended membranes. The eight microwells on the left are not covered by the film. The scale bar is  $20 \mu\text{m}$ . The top right inset shows an illustration of the sample. The bottom right inset shows an AFM line scan across the edge of a 35-nm-thick film, along the white line in the corresponding image. (c) SEM images of an intact (top) and a ruptured (bottom) 35-nm-thick membrane. The suspended region is false-colored in orange, and the rest is colored in blue. The scale bar is  $2 \mu\text{m}$ . (d) AFM line scans through the center of 35-nm-thick circular membranes of radius  $4.25 \mu\text{m}$  at atmospheric pressure. The data were taken within one hour after the membranes were removed from a high pressure chamber filled with nitrogen at 50 kPa (red) and 100 kPa (blue) above atmospheric pressure. Note the region adhered on the wall in the red curve.

substrate walls.

Figure 1b and 1c respectively show optical and scanning electron microscope (SEM) images of our nanomechanical drum resonators. Here, 2DPA-1 films are transferred onto  $\text{SiO}_2$  substrates via wet transfer [21]. The substrates have arrays of etched microwells with depths of  $g = 960 \text{ nm}$  and radii  $R$  of either  $4.25 \mu\text{m}$  or  $2.75 \mu\text{m}$ . In Figure 1b, the 2DPA-1 film partially covers the chip. The right insets show an illustration (top) and an AFM line scan (bottom) across the edge of the film. The SEM images in Figure 1c show an intact (top) and a broken (bottom) membrane with  $R = 4.25 \mu\text{m}$  and thickness  $h = 35 \text{ nm}$ .

The samples in this study are measured in two distinct pressure states: i) nearly flat with very low gas pressure on either side, and ii) bulged with finite gas pressure  $p_{in}$  inside the microwell and very low pressure  $p_{ext}$  outside. Although the membranes are highly impermeable [22], gas transport into and out-of the microwell can take place through the interface between the polymer film and the substrate [25–27]. When the samples are placed in a high pressure gas chamber ( $p_{ext} = 120 - 300 \text{ kPa}$ ), the gas leaks into the microwell through the interface [22]. Once the sample is transferred to a low pressure environment (vacuum chamber or atmosphere), the pressure difference,  $\Delta p = p_{in} - p_{ext}$ , across the membrane causes it to initially bulge up. Figure 1d shows two AFM line scans of membranes at atmospheric pressure shortly after removal from a high pressure chamber. When brought to atmospheric pressure, bulged membranes gradually deflate on timescales ranging from minutes to several years [22]. If the samples are put in a low pressure chamber (i.e.,  $p_{ext} \approx 0$ ), the gas inside the microwell eventually leaks out, allowing the membrane to deflate to a nearly flat state. When  $\Delta p = 0$ , the membrane may be partially

adhered to the inside wall of the microwell (Figure 1c) in a stretched configuration with tension. If  $\Delta p$  is increased, the membrane starts to delaminate from the wall (Figure 1d), which typically introduces some slack [28–30]. We analyze both states in systematic experiments below.

We first measure the Brownian motion, i.e., thermal displacement fluctuations, of nearly flat membranes in vacuum. We achieve the flat state by placing the samples into a chamber maintained at a vacuum of  $\sim 10^{-7} \text{ Torr}$  ( $10^{-5} \text{ Pa}$ ) by an ion pump, which results in  $p_{in} \approx p_{ext} \sim 10^{-7} \text{ Torr}$ . The membranes display detectable thermal resonances for the first few eigenmodes ( $m, n$ ) due to the relatively low dissipation with resonance frequencies  $f_{mn}$  and quality factors  $Q_{mn}$ . We use a path-stabilized homodyne Michelson interferometer to measure the thermal resonances at an antinode of each mode [31]. Details of the measurement process can be found in the Supporting Information file. Figure 2a shows the power spectral density (PSD) of the displacement fluctuations of the first four eigenmodes of a membrane with  $R = 4.25 \mu\text{m}$  and  $h = 35 \text{ nm}$ . For  $m \neq 0$ , two nominally degenerate modes exist. If the resonator geometry deviates from an ideal circle, the resonance frequencies of these modes can split — as noticeable for the modes (1, 1) and (2, 1) in Figure 2a. The split modes can be clearly resolved by changing the angular position of the laser spot on the membrane. We fit each peak with a Lorentzian curve to determine  $f_{mn}$  and  $Q_{mn}$ .

To analyze the eigenfrequencies, we turn to the equation for the free transverse vibrations of a uniform circular plate under tension with radius  $R$ , thickness  $h$ , density  $\rho$ , tension  $S$ , and bending stiffness  $D = \frac{Eh^3}{12(1-\nu^2)}$ , where  $E$  is the Young's modulus and  $\nu$  is the Poisson's ratio:

$$\rho h \frac{\partial^2 W}{\partial t^2} + \frac{D}{R^4} \nabla^4 W - \frac{S}{R^2} \nabla^2 W = 0. \quad (1)$$

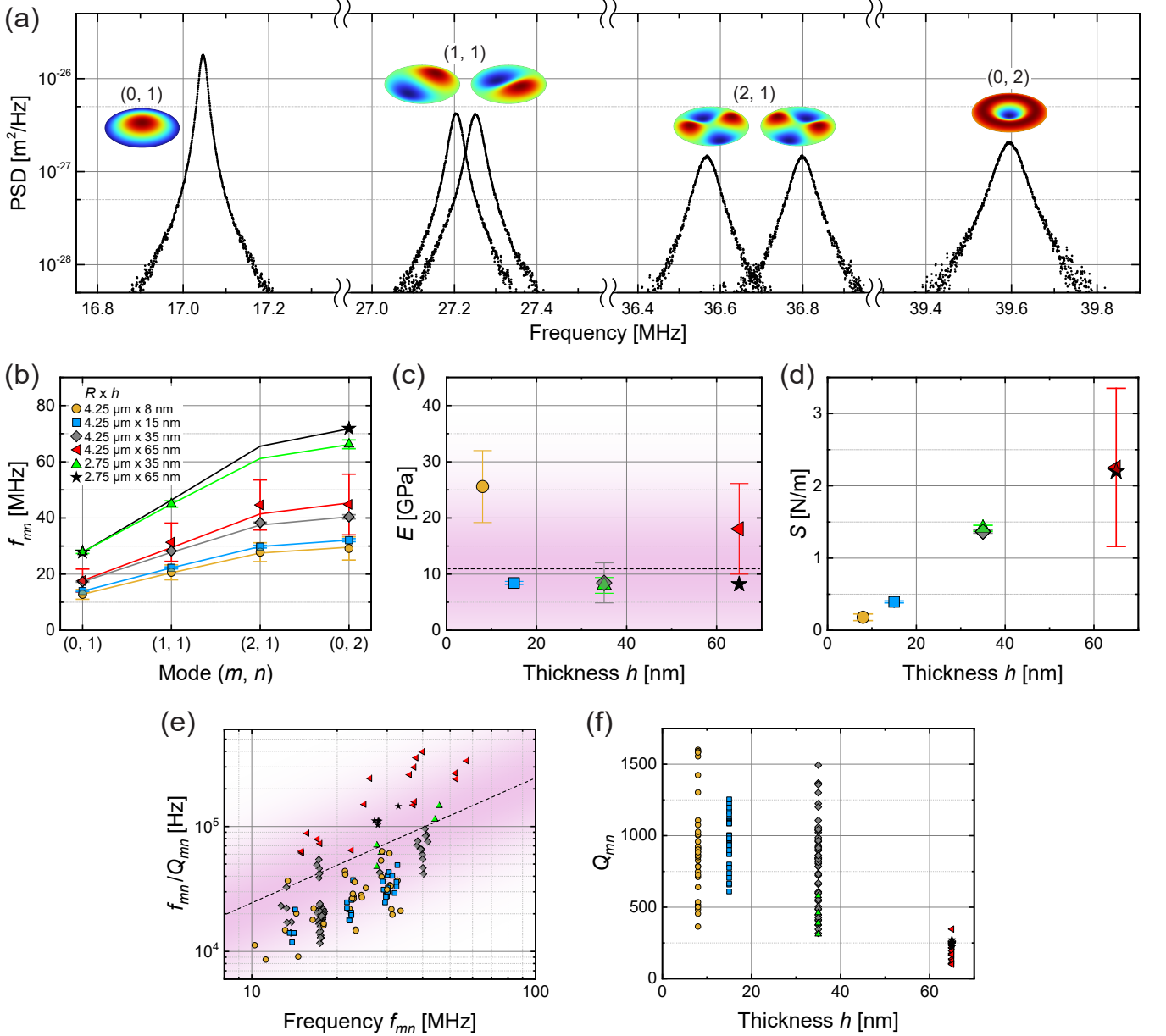


FIG. 2. (a) PSD of displacement fluctuations of the first four modes of a membrane with  $R = 4.25 \mu\text{m}$  and  $h = 35 \text{ nm}$ . (b) Resonance frequencies  $f_{mn}$  for membranes with indicated  $R$  and  $h$ . The lines show the theoretical frequencies of the first four modes calculated using Eq. (2). (c) Young's modulus  $E$  and (d) tension  $S$  of the membranes shown in (b) as a function of thickness  $h$ . The dashed line and the shading respectively indicate the mean and spread of data with the Young's modulus being  $E = 11.2 \pm 8.8 \text{ GPa}$ . (e) Dissipation constants  $\frac{f_{mn}}{Q_{mn}}$  as a function of frequency for all measured modes. The shading highlights that  $\frac{f_{mn}}{Q_{mn}} \propto f_{mn}$ , and the dashed line is a linear fit through the origin. (f) Quality factors  $Q_{mn}$  of all measured modes as a function of 2DPA-1 thickness.

Here,  $\nabla^2$  is the Laplacian operator in cylindrical coordinates;  $\nabla^4 = (\nabla^2)^2$ ; and  $W(r, \theta)$  is the displacement at  $(r, \theta)$ . The coordinate  $r$  has been normalized with  $R$  such that  $0 \leq r \leq 1$ . A dimensionless tension parameter  $U = \frac{SR^2}{D} = \frac{12(1-\nu^2)SR^2}{Eh^3}$  emerges from Eq. (1) with the plate and membrane limits for  $U \rightarrow 0$  and  $U \rightarrow \infty$ , respectively. Under clamped boundary conditions, Eq. (2)

yields the resonance frequency of each eigenmode as [32]

$$f_{mn} = \frac{\alpha_{mn}}{2\pi R} \sqrt{\frac{1}{\rho h}} \sqrt{S + \frac{\alpha_{mn}^2 D}{R^2}}. \quad (2)$$

The coefficient  $\alpha_{mn}$  corresponds to the  $n^{\text{th}}$  root of

$$\alpha \frac{J_{m+1}(\alpha)}{J_m(\alpha)} + \beta \frac{I_{m+1}(\beta)}{I_m(\beta)} = 0, \quad (3)$$

where  $J_m$  and  $I_m$  are the regular and modified Bessel functions of the first kind, respectively, and  $\beta = \sqrt{\alpha^2 + SR^2/D}$ . As  $U$  becomes large, e.g., due to a large  $S$  or small  $h$ , the bending term drops out of Eq. (1), yielding the membrane eigenfrequencies

$$f_{mn} = \frac{\alpha'_{mn}}{2\pi R} \sqrt{\frac{S}{\rho h}}, \quad (4)$$

where  $\alpha'_{mn}$  is the  $n^{\text{th}}$  root of the Bessel function  $J_m$  [33].

Figure 2b shows the resonance frequencies of multiple modes of membranes with different  $R$  and  $h$ . Each data point is obtained by averaging measurements from  $1 \leq N \leq 10$  membranes on the same chip with the same linear dimensions. Tables S1-3 in the Supporting Information file list all measured  $f_{mn}$  and  $Q_{mn}$ . For some membranes, not all modes could be resolved due to low  $Q$  values and, in the case of smaller membranes, small displacement amplitudes.

As long as the frequencies of two modes of the same membrane are measured, we can find  $E$  and  $S$  by performing error minimization in a parametric sweep [31, 34]. For each possible combination of  $E$  and  $S$ , we calculate  $\alpha_{mn}$  from Eq. (3) and the theoretical eigenfrequencies  $f_{mn}^{(t)}$  from Eq. (2) for the first four eigenmodes. We then minimize the error between the experimental and theoretical frequencies as described in the Supporting Information file to find the  $E$  and  $S$  values. Figure 2c and d respectively show the  $E$  and  $S$  found from error minimization. Returning to Figure 2b, the lines show the theoretical  $f_{mn}$  based on the mean  $E$  and  $S$  values for a given  $R$  and  $h$ ; the agreement is very good. The values for  $E$ ,  $S$ , and  $U$ , as well as the number  $N$  of resonators measured for each combination of  $R$  and  $h$  are listed in Table I. The resonators with  $h = 65$  nm have large error bars for  $E$  and  $S$  due to the small sample size. For the resonators with  $h = 8$  nm, the rigidity term in Eq. (2) becomes small compared to the tension term, thus making the tension term dominant and the estimate for  $E$  error-prone. In summary, we find the average value  $E = 11.2 \pm 8.8$  GPa, which is in good agreement with  $E = 12.7 \pm 3.8$  GPa obtained from nanoindentation measurements [21]. We also extracted  $E$  and  $S$  using a different approach but arrived at similar values, as described in the Supporting Information file.

Figure 2e shows the dissipation constant,  $\frac{f_{mn}}{Q_{mn}}$ , for all the measured modes. Even though there is spread in the data from different modes and devices, the dissipation constant seems to increase linearly with frequency, indicating that  $Q_{mn}$  is frequency independent. It has been argued [35] that surface and bulk dissipation respectively result in  $Q$  factors that should scale as  $Q \propto h$  and  $Q \propto \text{constant}$ . In an effort to observe one of these trends, we plot all  $Q_{mn}$  data as a function of  $h$  (Figure 2f). The thickest polymer devices appear to have the lowest  $Q$  factors, although further experiments are needed for a conclusive statement.

TABLE I. Radius  $R$ , thickness  $h$ , Young's modulus  $E$ , tension  $S$ , and non-dimensional tension parameter  $U$  of the resonators in Figure 2b-d. The data are from  $N$  different resonators on the same chip.

$R \times h$ [ $\mu\text{m} \times \text{nm}$ ]	$E$ [GPa]	$S$ [N/m]	$U$ [ $\cdot$ ]	$N$
$4.25 \times 8$	$25.58 \pm 6.40$	$0.18 \pm 0.05$	$3 \times 10^3$	6
$4.25 \times 15$	$8.42 \pm 0.28$	$0.39 \pm 0.01$	$3 \times 10^3$	5
$4.25 \times 35$	$8.44 \pm 3.55$	$1.37 \pm 0.02$	$8 \times 10^2$	10
$4.25 \times 65$	$18.07 \pm 8.06$	$2.26 \pm 1.09$	$9 \times 10^1$	3
$2.75 \times 35$	$8.80 \pm 1.40$	$1.41 \pm 0.04$	$4 \times 10^2$	3
$2.75 \times 65$	8.20	2.20	$9 \times 10^1$	1

To gain more insight into the effect of wall adhesion and delamination on the resonance frequency, we perform a second set of experiments with bulged membranes. First, we describe our model for the resonance of a bulged and partially adhered membrane. The illustration in Figure 3a shows three snapshots of the membrane cross-section along with the relevant coordinates, including the experimental time coordinate. Our mechanical model does not distinguish between inflating and deflating membranes, and we prefer to describe the phenomenon beginning with the final state (backward in time). At its final flat state ( $\Delta p = p_{in} - p_{out} = 0$ ), the membrane is re-adhered to the inner wall of the microwell at  $z = 0$ . The  $z_1$  level is selected such that the tension in the membrane becomes zero if the membrane is flat at  $z_1$ . As the membrane separates from the wall starting at  $z = 0$  toward  $z_1$  due to  $\Delta p > 0$ , it maintains some of the initial tension and acquires some additional tension due to the bulging, with  $\delta_c$  being the bulge height at the center with respect to  $z = 0$ . When the membrane is at  $z_1$ , the tension is entirely due to bulging. Further delamination causes a slack being introduced into the membrane, which results in an increased  $\delta_c$ . The tension in the membrane in these regimes is derived from a spherical cap model in the Supporting Information file and can be summarized as

$$S^*(z^*) = \begin{cases} z_1^* & \text{for } z^* = 0, \\ (z_1^* - z^*) + \frac{2}{3}(\delta_c^* - z^*)^2 & \text{for } 0 < z^* \leq z_1^*, \\ (z_1^* - z^*) + \frac{2}{3}(1 - z^* + z_1^*)(\delta_c^* - z^*)^2 & \text{for } z^* > z_1^*. \end{cases} \quad (5)$$

Here, we present the results in dimensionless form, where  $S^*(z^*) = \frac{S(z^*)}{Bh}$ , with  $B = \frac{E}{1-\nu}$  being the biaxial modulus; the dimensionless length scales are  $\delta_c^* = \frac{\delta_c}{R}$ ,  $z^* = \frac{z}{R}$ , and  $z_1^* = \frac{z_1}{R}$ . Using  $S(z)$  in Eqs. (3) and (2) along with  $E$ ,  $\rho$ ,  $\nu$ , and linear dimensions provides the resonance frequency of the bulged-up and delaminated membrane. We reemphasize that the model does not depend on the direction of time.

In our re-adhesion experiments, the membranes are put into a high pressure chamber filled with nitrogen at  $p_{ext} = 200$  kPa for several days before being placed

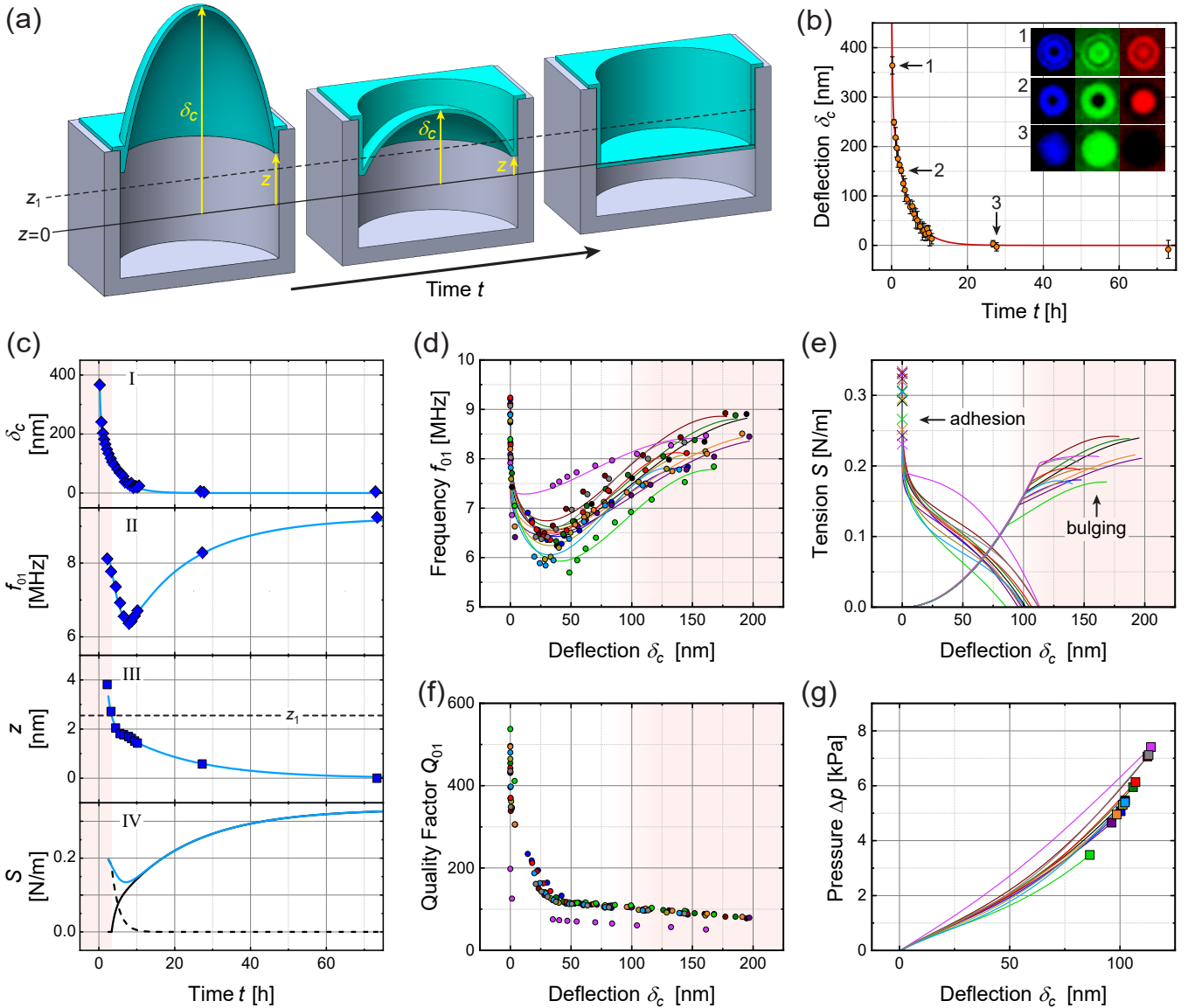


FIG. 3. (a) Illustration of a membrane at different stages of bulging. Note the time coordinate of our experiments. When  $\Delta p = 0$  (right), the membrane is flat at  $z = 0$  and stretched. For  $\Delta p > 0$  (middle), the membrane is adhered to the wall to position  $z > 0$  and bulges up by  $\delta_c - z$ . For  $z > z_1$  (left), slack is introduced. Note that the illustration is not to scale; in the experiments,  $z \ll \delta_c$ . (b) Measured center deflection  $\delta_c$  for a 35-nm-thick membrane with  $R = 4.25 \mu\text{m}$  over time. The  $\delta_c = 0$  line corresponds to the flat membrane at  $z = 0$ . The inset shows interferograms at wavelengths of 440 nm (blue), 540 nm (green), and 600 nm (red) for different  $\delta_c$  as indicated by the arrows. (c) Time-dependent  $\delta_c$ ,  $f_{01}$ ,  $z$ , and tension  $S$  for a 35-nm thick membrane. The shown values for  $z$  are calculated from measurements. The fit for  $z$  is an exponential function with two time constants, which is used to calculate the continuous curve in the frequency plot. The dashed line corresponds to the delamination length  $z_1$  below which there is no slack. The total tension  $S$  (blue line) is comprised of a component due to bulging (black dashed line) and one due to wall adhesion (black solid line). The shading indicates the region of slack in the membrane. (d) Experimental data (symbols) and fits (lines) for  $f_{01}$  as a function of  $\delta_c$  for twelve 35-nm-thick membranes, including the one in (c). The shaded regions indicate the range where slack exists in the membrane. (e) Tension components caused by bulging and wall adhesion as a function of  $\delta_c$ , with the symbols representing the calculated tension at  $z = 0$ . (f) Quality factors  $Q_{01}$  as a function of  $\delta_c$ . (g) Pressure  $\Delta p$  in the regime without slack ( $z \leq z_1$ ) as a function of  $\delta_c$ .

into the vacuum chamber ( $p_{ext} \approx 0$ ). We measure the fundamental resonance frequency  $f_{01}$  and the quasistatic deflection field simultaneously as gas leaks out of the microwell slowly as a function of time. The deflection field is measured using full-field interferometry [36] with the

details given in the Supporting Information file. In the experiments, the membrane starts in a bulged-up and delaminated state (Figure 3a left). As the gas leaks out of the microwell, the membrane slowly deflates until the final flat state is reached (Figure 3a right). Figure 3b

shows the measured deflection  $\delta_c$  at the center of a 35-nm-thick membrane over time, which can be fitted with an exponential decay function with two time constants. The asymptote corresponds to a flat membrane ( $\delta_c = 0$ ,  $z = 0$ ).

Figure 3c shows measured  $\delta_c$  and  $f_{01}$  of a 35-nm-thick membrane as a function of time. Also shown are the calculated position  $z$  of the membrane on the wall, and the tension  $S$ . The analysis is performed as follows. At the last data point ( $t \approx 75$  h), we assume  $z = 0$  and determine  $S(0)$  from the measured  $f_{01}$  using Eqs. (2) and (3) with  $E = 12.7$  GPa and  $\nu = 0.2$ . Then, we find the value for  $z_1$  as  $\frac{Bh z_1}{R} = S(0)$ . Once  $z_1$  is found, we work our way through the rest of the frequency measurements with  $\delta_c > 0$  and  $z > 0$ . We note that  $f_{01}$  depends on  $S$  through Eqs. (3) and (2);  $S$ , in turn, depends on  $z$ ,  $\delta_c$  and  $z_1$  through Eq. (5). Thus, we can determine the  $z$  value for each  $f_{01}$  based on the measured  $\delta_c$  and  $z_1$  (Figure 3c III). The data points for  $z$  can be fitted with an exponential function with two time constants, which in turn allows us to generate continuous curves for other parameters. With  $z$ ,  $\delta_c$  and Eq. (5), we also determine the contributions of the tension terms (Figure 3c IV) due to bulging (dotted line) and due to wall adhesion (continuous black line).

Figure 3d shows the fundamental frequencies  $f_{01}$  of twelve 35-nm-thick membranes as a function of  $\delta_c$ . The continuous curves are found from the model as described above, but plotted as a function  $\delta_c$  instead of time. The respective contributions of the two tension terms are shown in Figure 3e. The sudden change in the slope of the bulging plots occurs at  $z = z_1$  when slack is introduced to the system. Figure 3f shows the quality factors  $Q_{01}$  of the same twelve membranes. As the membranes deflate,  $Q_{01}$  increases due to decreased gas damping and increased tension due to adhesion.

Next, we estimate the pressure inside the microwell by focusing on the regime without slack ( $0 \leq z \leq z_1$ ). In this regime,  $\Delta p = p_{in} - p_{out} \approx p_{in}$  and can be determined as

$$\Delta p = Bh^*(\delta_c^* - z^*) \times \left[ \frac{8}{3}(\delta_c^* - z^*)^2 + 4(z_1^* - z^*) + \frac{16}{3(1+\nu)}h^{*2} \right], \quad (6)$$

where  $h^* = \frac{h}{R}$ . The derivation for Eq. (6) can be found in the Supporting Information file. Figure 3g shows  $\Delta p$  as a function of  $\delta_c$ .

Finally, the energy of adhesion of the membrane to the substrate can also be estimated, but only at the limit of a flat membrane, i.e.,  $z \approx 0$ . At equilibrium, the total free energy change is

$$\frac{dW}{dz} + \frac{dF_s}{dz} + \frac{dF_a}{dz} = 0, \quad (7)$$

where all  $z$  derivatives are evaluated at  $z = 0$ . Here,  $\frac{dW}{dz}$  is the incremental work done by the gas inside the microwell on the membrane;  $F_s$  is the strain energy stored

in the membrane;  $F_a$  is the free energy of adhesion. Figure 3g shows that  $\frac{dW}{dz} = -\Delta p \frac{dV}{dz} \approx 0$ , with  $V_b$  being the volume of the bulge, because  $\Delta p \approx 0$  at  $z = 0$ . The strain energy is entirely due to the tension caused by wall adhesion [37],

$$F_s(z) \approx \pi B h (z_1 - z)^2, \quad (8)$$

and  $\frac{dF_a}{dz} = 2\pi R \Gamma$  where  $\Gamma$  is the adhesion energy per unit area. Thus, in the limit of  $z \approx 0$ , this free energy model simply yields  $\Gamma = Bh \frac{z_1}{R} = S(0)$ . We find the average value of  $\Gamma = 0.29 \pm 0.04$  J/m<sup>2</sup>.

The value for  $S(0)$  and, therefore,  $\Gamma$  is lower for the deflating membranes (Figure 3e) compared to those that were never bulged by pressurization (Figure 2d). This observation can be explained by the history-dependence of the separation-adhesion process: hysteresis has been observed in separation-adhesion experiments on other 2D materials, where the energy of separation is significantly larger than the energy of adhesion [38]. In our experiments on deflating membranes (Figure 3), we essentially measure the energy of re-adhesion of a membrane that was previously adhered to the substrate and then separated. The data in Figure 2 are on membranes that were never separated. It appears that after separation, the membranes do not adhere as strongly, leading to smaller values of tension in their final states. Consistent with this, the deflated membranes in Figure 3f exhibit lower  $Q_{01}$  values at  $\delta_c = 0$  compared with flat membranes of the same radius and thickness that were never pressurized (Figure 2f). Because of higher tension, the resonance frequencies in Figure 2b are typically higher compared to those in Figure 3d, which also results in higher quality factors due to dissipation dilution [39].

We assume that equilibrium exists as the membranes re-adhere to the sidewalls of the microwell in the deflation experiments of Figure 3. Here, we take a continuum view of the polymeric material, even though there may be rearrangements in the molecular-scale disks making up the membrane, leading to entropy changes. This is unlike the situation in 2D crystalline materials, such as graphene, and makes the equilibrium in the system more interesting from a fundamental perspective.

In conclusion, we have explored the device possibilities of a novel 2D material, 2DPA-1, by fabricating and measuring nanomechanical resonators with molecular thicknesses; we have also extracted its material properties and developed complex nanomechanical resonance models with slack and adhesion. Our  $\Gamma$  value for the adhesion of 2DPA-1 on SiO<sub>2</sub> is close to those reported for 2D crystalline materials, such as graphene [40] and MoS<sub>2</sub> [38]. The Young's modulus of 2DPA-1, on the other hand, is one to two orders of magnitude smaller [41, 42]. It remains an open question whether other properties of 2DPA-1 match conventional 1D polymers or crystalline 2D materials.

## SUPPORTING INFORMATION

Additional experimental details on resonance and deflection measurements; information on frequency stability; derivation of the spherical-cap model for delaminating membranes; further information on the determination of material properties; and supporting data tables.

## ACKNOWLEDGMENTS

We acknowledge support from the US NSF (Grant Nos. CMMI-2001403, CMMI-1934271, and CMMI-2337507). Polymer syntheses and fabrication of pressurized bulge devices were supported by the Center for Enhanced Nanofluidic Transport–Phase 2 (CENT<sup>2</sup>), an Energy Frontier Research Center funded by the US Department of Energy, Office of Science, Basic Energy Sciences (Grant No. DE-SC0019112).

## REFERENCES

- [1] A. N. Cleland and M. L. Roukes, Fabrication of high frequency nanometer scale mechanical resonators from bulk Si crystals, *Appl. Phys. Lett.* **69**, 2653 (1996).
- [2] D. Carr and H. Craighead, Fabrication of nanoelectromechanical systems in single crystal silicon using silicon on insulator substrates and electron beam lithography, *J. Vac. Sci. Technol. B* **15**, 2760 (1997).
- [3] T. Yildirim, L. Zhang, G. P. Neupane, S. Chen, J. Zhang, H. Yan, M. M. Hasan, G. Yoshikawa, and Y. Lu, Towards future physics and applications via two-dimensional material NEMS resonators, *Nanoscale* **12**, 22366 (2020).
- [4] B. Xu, P. Zhang, J. Zhu, Z. Liu, A. Eichler, X.-Q. Zheng, J. Lee, A. Dash, S. More, S. Wu, Y. Wang, H. Jia, A. Naik, A. Bachtold, R. Yang, P. X.-L. Feng, and Z. Wang, Nanomechanical resonators: toward atomic scale, *ACS Nano* **16**, 15545 (2022).
- [5] P. F. Ferrari, S. Kim, and A. M. van der Zande, Nanoelectromechanical systems from two-dimensional materials, *Appl. Phys. Rev.* **10** (2023).
- [6] J. S. Bunch, A. M. Van Der Zande, S. S. Verbridge, I. W. Frank, D. M. Tanenbaum, J. M. Parpia, H. G. Craighead, and P. L. McEuen, Electromechanical resonators from graphene sheets, *Science* **315**, 490 (2007).
- [7] S. J. Cartamil-Bueno, M. Cavalieri, R. Wang, S. Hour, S. Hofmann, and H. S. van der Zant, Mechanical characterization and cleaning of CVD single-layer h-BN resonators, *npj 2D Mater. Appl.* **1**, 16 (2017).
- [8] J. Lee, Z. Wang, K. He, J. Shan, and P. X.-L. Feng, High frequency MoS<sub>2</sub> nanomechanical resonators, *ACS Nano* **7**, 6086 (2013).
- [9] C.-H. Liu, I. S. Kim, and L. J. Lauhon, Optical control of mechanical mode-coupling within a MoS<sub>2</sub> resonator in the strong-coupling regime, *Nano Lett.* **15**, 6727 (2015).
- [10] B. Xu, J. Zhu, F. Xiao, N. Liu, Y. Liang, C. Jiao, J. Li, Q. Deng, S. Wu, T. Wen, S. Pei, H. Wan, X. Xiao, J. Xia, and Z. Wang, Electrically tunable MXene nanomechanical resonators vibrating at very high frequencies, *ACS Nano* **16**, 20229 (2022).
- [11] F. Ye, A. Islam, T. Zhang, and P. X.-L. Feng, Ultra-wide frequency tuning of atomic layer van der Waals heterostructure electromechanical resonators, *Nano Lett.* **21**, 5508 (2021).
- [12] P. Kanjanaboos, X.-M. Lin, J. E. Sader, S. M. Rupich, H. M. Jaeger, and J. R. Guest, Self-assembled nanoparticle drumhead resonators, *Nano Lett.* **13**, 2158 (2013).
- [13] S. Markutsya, C. Jiang, Y. Pikus, and V. V. Tsukruk, Freely suspended layer-by-layer nanomembranes: testing micromechanical properties, *Adv. Funct. Mater.* **15**, 771 (2005).
- [14] X. Wang, T. Yildirim, K. J. Si, A. Sharma, Y. Xue, Q. Qin, Q. Bao, W. Cheng, and Y. Lu, An adaptive soft plasmonic nanosheet resonator, *Laser Photonics Rev.* **13**, 1800302 (2019).
- [15] A. W. McFarland, M. A. Poggi, L. A. Bottomley, and J. S. Colton, Injection moulding of high aspect ratio micron-scale thickness polymeric microcantilevers, *Nanotechnology* **15**, 1628 (2004).
- [16] J. Bunyan and S. Tawfick, Mechanical behavior of PDMS at low pressure, *Mater. Res. Express* **4**, 075306 (2017).
- [17] A. Gaitas and Y. B. Gianchandani, An experimental study of the contact mode AFM scanning capability of polyimide cantilever probes, *Ultramicroscopy* **106**, 874 (2006).
- [18] Y. Yoon, I. Chae, T. Thundat, and J. Lee, Hydrogel microelectromechanical system (MEMS) resonators: beyond cost-effective sensing platform, *Adv. Mater. Technol.* **4**, 1800597 (2019).
- [19] G. Zhang, J. Gaspar, V. Chu, and J. Conde, Electrostatically actuated polymer microresonators, *Appl. Phys. Lett.* **87** (2005).
- [20] U. Adiyan, T. Larsen, J. J. Zárate, L. G. Villanueva, and H. Shea, Shape memory polymer resonators as highly sensitive uncooled infrared detectors, *Nat. Commun.* **10**, 4518 (2019).
- [21] Y. Zeng, P. Gordiichuk, T. Ichihara, G. Zhang, E. Sandoz-Rosado, E. D. Wetzel, J. Tresback, J. Yang, D. Kozawa, Z. Yang, M. Kuehne, M. Quien, Z. Yuan, X. Gong, G. He, D. J. Lundberg, P. Liu, A. T. Liu, J. F. Yang, H. J. Kulik, and M. S. Strano, Irreversible synthesis of an ultrastrong two-dimensional polymeric material, *Nature* **602**, 91 (2022).
- [22] C. L. Ritt, M. Quien, Z. Wei, H. Gress, M. Dronadula, K. Altmisdort, Y.-M. Tu, M. Gadalooff, N. Aluru, K. L. Ekinci, J. S. Bunch, and M. S. Strano, A molecularly impermeable polymer from two-dimensional polyaramids, *Nature* **647**, 383 (2025).
- [23] X. Zhuang, Y. Mai, D. Wu, F. Zhang, and X. Feng, Two-dimensional soft nanomaterials: a fascinating world of

materials, *Adv. Mater.* **27**, 403 (2015).

[24] Y. Ren and Y. Xu, Recent advances in two-dimensional polymers: synthesis, assembly and energy-related applications, *Chem. Soc. Rev.* (2024).

[25] M. Lee, D. Davidovikj, B. Sajadi, M. Šiškins, F. Alijani, H. S. Van Der Zant, and P. G. Steeneken, Sealing graphene nanodrums, *Nano Lett.* **19**, 5313 (2019).

[26] Y. Manzanares-Negro, P. Ares, M. Jaafar, G. López-Polín, C. Gómez-Navarro, and J. Gómez-Herrero, Improved graphene blisters by ultrahigh pressure sealing, *ACS Appl. Mater. Interfaces* **12**, 37750 (2020).

[27] H. R. Ambjørner, A. S. Bjørnlund, T. G. Bonczyk, E. Dollekamp, L. M. Kaas, S. Colding-Fagerholt, K. S. Mølhave, C. D. Damsgaard, S. Helveg, and P. C. K. Vesborg, Thermal dynamics of few-layer-graphene seals, *Nanoscale* **15**, 16896 (2023).

[28] J. S. Bunch, S. S. Verbridge, J. S. Alden, A. M. Van Der Zande, J. M. Parpia, H. G. Craighead, and P. L. McEuen, Impermeable atomic membranes from graphene sheets, *Nano Lett.* **8**, 2458 (2008).

[29] M. Calis, D. Lloyd, N. Boddeti, and J. S. Bunch, Adhesion of 2D MoS<sub>2</sub> to graphite and metal substrates measured by a blister test, *Nano Lett.* **23**, 2607 (2023).

[30] G. Cao and F. An, An innovative approach to characterize the elastic moduli of 2D materials from the central strain of bulged membrane, *Int. J. Mech. Sci.* **274**, 109254 (2024).

[31] H. Gress, J. Barbish, C. Yanik, I. Kaya, R. Erdogan, M. Hanay, M. González, O. Svitelskiy, M. Paul, and K. Ekinci, Multimode Brownian dynamics of a nanomechanical resonator in a viscous fluid, *Phys. Rev. Appl.* **20**, 044061 (2023).

[32] T. Wah, Vibration of circular plates, *J. Acoust. Soc. Am.* **34**, 275 (1962).

[33] W. Weaver Jr, S. P. Timoshenko, and D. H. Young, *Vibration problems in engineering* (John Wiley & Sons, 1991).

[34] A. B. Ari, M. S. Hanay, M. R. Paul, and K. L. Ekinci, Nanomechanical measurement of the Brownian force noise in a viscous liquid, *Nano Lett.* **21**, 375 (2020).

[35] K. Y. Yasumura, T. D. Stowe, E. M. Chow, T. Pfafman, T. W. Kenny, B. C. Stipe, and D. Rugar, Quality factors in micron-and submicron-thick cantilevers, *J. Microelectromech. Syst.* **9**, 117 (2000).

[36] L. Lipiäinen, K. Kokkonen, and M. Kaivola, Homodyne full-field interferometer for measuring dynamic surface phenomena in microstructures, *Opt. Lasers Eng.* **88**, 178 (2017).

[37] S. Timoshenko, *Theory of plates and shells* (McGraw-Hill, 1959).

[38] D. Lloyd, X. Liu, N. Boddeti, L. Cantley, R. Long, M. L. Dunn, and J. S. Bunch, Adhesion, stiffness, and instability in atomically thin MoS<sub>2</sub> bubbles, *Nano Lett.* **17**, 5329 (2017).

[39] N. J. Engelsen, A. Beccari, and T. J. Kippenberg, Ultrahigh-quality-factor micro-and nanomechanical resonators using dissipation dilution, *Nat. Nanotechnol.* **19**, 725 (2024).

[40] S. P. Koenig, N. G. Boddeti, M. L. Dunn, and J. S. Bunch, Ultrastrong adhesion of graphene membranes, *Nat. Nanotechnol.* **6**, 543 (2011).

[41] C. Lee, X. Wei, J. W. Kysar, and J. Hone, Measurement of the elastic properties and intrinsic strength of monolayer graphene, *Science* **321**, 385 (2008).

[42] A. Castellanos-Gomez, M. Poot, G. A. Steele, H. S. van der Zant, N. Agraít, and G. Rubio-Bollinger, Elastic properties of freely suspended MoS<sub>2</sub> nanosheets, *Adv. Mater.* **24**, 772 (2012).